Intermittent Sinusoidal Modulation of Bidirectional Series Resonant Converter With Zero Current Switching, Linear Current Controllability, and Load-Independent Efficiency

Zhijian Fang, *Member, IEEE*, Hanlin Dong, Haotian Sun, Fei Xie, and Zhicong Huang, *Member, IEEE*

***Abstract*—Sinusoidal modulation can keep the resonant current in phase with the terminal voltage, and, thus, it is feasible to achieve both zero current switching (ZCS) ON/OFF and eliminate backflow power in a series resonant converter. However, it makes the transfer characteristics inherently dependent on the resonant tank and, thus, challenges power regulation. In this article, a novel intermittent sinusoidal modulation is proposed for a bidirectional series resonant converter (BSRC). Each switching cycle incorporates a sinusoidally modulated resonant period and an intermittent period for the current controllability, while fully ZCS as well as null backflow power can be maintained for high efficiency regardless of load conditions. The BSRC operates as a current source, with the normalized voltage gain being either stepped up or down, to achieve a wide range of output power. Moreover, the output power together with the power loss is proportional to the switching frequency, making the high power efficiency independent of the load. Therefore, fully ZCS, linear current controllability, and load-independent high efficiency can be simultaneously realized throughout a wide load range. A 1-kVA BSRC prototype that interfaces a high-voltage bus ranging from 240 to 480 V and a low-voltage bus of 48 V validates the proposed modulation scheme.**

***Index Terms*—Bidirectional series resonant converter (BSRC), current controllability, efficiency, soft switching, wide range.**

I. Introduction

BATTERY energy systems are regarded as short-term or long-term energy buffers to stabilize the energy transfer in applications of renewable energy as well as electric vehicle [1]–[3]. A bidirectional dc/dc converter is essential in the battery energy system, which connects the high-voltage dc bus and charges/discharges the battery [4], [5]. In a typical charging and discharging profile of a Li-ion battery cell [6], the cell voltage ranges from a discharging cutoff value of 2.7 V to a charging threshold value of 4.2 V, while the charging and discharging currents can vary from its rated value to a few percentages of the rated value. Such that, the dc/dc converter is expected to have a wide operation range, i.e., wide-range voltage gain as well as wide-range output power. Moreover, high efficiency throughout the whole operation range is also desired to reduce power loss during the energy exchange.

Bidirectional series resonant converters (BSRCs) are widely used to interconnect the Li-ion batteries and the high voltage dc buses. Although the wide operating range and high efficiency are usually desired [7], [8], modulation schemes that can achieve these features are challenging. Variable frequency modulation (VFM) is widely used to regulate the output power while ensuring zero voltage switching (ZVS) in the inverter and zero current switching (ZCS) in the rectifier [9]. However, the VFM-controlled BSRC can only work as a buck converter, and its voltage gain is insensitive to the switching frequency, which leads to a restricted operating range [10], [11]. Alternatively, the output power can be regulated by adjusting the voltage phase angle between the inverter and the rectifier, which is called phase-shift modulation (PSM). Although PSM enables power regulation in a wide voltage gain range, there exists a large circulating current and the backflow power increasing the conduction loss [12], [13]. Pulsewidth modulation can help minimize the circulating current [14]–[20], but the switches suffer from hard turn-ON/OFF, leading to significant switching loss and electromagnetic interference (EMI) noise. VFM+PSM methods are proposed to achieve soft switching over a wide operating range [21], with a penalty of increasing the circulating current. Then, a four degrees-of-freedom modulation (FDM) is proposed [22], [23], which controls the switching frequency, duty cycle, and shifting phase simultaneously to reduce the circulating current and achieve ZVS-ON for a wide operating range. Nevertheless, the complex and nonlinear relationship between the frequency, duty cycle, and shifting phase makes the

Manuscript received November 11, 2021; revised February 11, 2022 and March 29, 2022; accepted May 8, 2022. Date of publication May 11, 2022; date of current version June 24, 2022. This work was supported in part by the National Natural Science Foundation of China under Grant 51707138 and Grant 52007067, in part by the Natural Science Foundation of Guangdong Province under Grant 2022A1515011581, and in part by the Guangzhou Municipal Science and Technology Bureau under Grant 202102020381. Recommended for publication by Associate Editor Diego G. Lamar. *(Corresponding author: Zhicong Huang.)*

Zhijian Fang, Hanlin Dong, Haotian Sun, and Fei Xie are with the School of Automation, China University of Geosciences (Wuhan), Wuhan 430074, China, and also with the Hubei Key Laboratory of Advanced Control and Intelligent Automation for Complex Systems, Wuhan 430074, China (e-mail: fangzj@cug.edu.cn; donghanlin@cug.edu.cn; finnick99@cug.edu.cn; mail_xiefei@cug.edu.cn).

Zhicong Huang is with the Shien-Ming Wu School of Intelligent Engineering, South China University of Technology, Guangzhou 510006, China (e-mail: zhiconghuang@scut.edu.cn).

Color versions of one or more figures in this article are available at https://doi.org/10.1109/TPEL.2022.3174390.

Digital Object Identifier 10.1109/TPEL.2022.3174390

controller design very difficult. Even though the large hard-ON loss of MOSFET in these modulations is avoided due to ZVS, the BSRC still suffers from hard-OFF, which increases with the turn-OFF current as well as the switching frequency. In summary, although modulation schemes in the literature have made the effort to extend the operation range and improve the efficiency, they fail to maintain high efficiency throughout the whole load range; specifically, efficiency deviation still exists in light load conditions.

When the switching frequency is fixed to the resonant frequency, named sinusoidal modulation, a sinusoidal resonant current in phase with the voltage can be provided, realizing ZCS-ON/OFF simultaneously [4], [24]. The ZCS-ON/OFF features are independent of the load conditions and can significantly alleviate the switching loss for a wide load range. However, since the operating frequency is fixed at the resonant frequency, the transfer characteristic is inherent and cannot satisfy the required wide operating range, unless the modulation scheme is further modified. An intermittent operation, also called ON/OFF control, is proposed by modifying a ratio of power-transfer interval with respect to nonpower-transfer interval to adjust the average delivered power [25]. Many control methods share the idea of the intermittent operation, such as burst control [26], [27] and pulse density modulation [28]. However, such methods can be only used for light load conditions limiting the operating range. Moreover, the ratio of nonpower-transfer interval with respect to a resonant period is usually a scalar integer, which reduces the operating range and the regulation resolution. Otherwise, large hard-OFF loss and EMI noise occur when the converter is turned OFF.

Other than the conventional methods, modulations using switching frequency lower than the resonant frequency are proposed to achieve ZCS-ON/OFF and extend the operating range. In [29], the switching cycle is multiple times of the resonant cycle, providing sinusoidal current at the resonant frequency, but the backflow power exists. To address the backflow power, discontinuous current mode sinusoidal modulation is proposed for the BSRC [30]. The switching frequency is also lower than the resonant frequency, but the resonant current waveform is sinusoidal for half-resonant cycle and discontinuous for the remaining half-switching period. Soft switching and regulated power can be both achieved. With such a modulation scheme, the BSRC is unidirectional and restricted to Buck conversion only in these modulations with lower switching frequency. Moreover, the output characteristic is nonlinearly dependent on the load, which makes the controller design difficult. Last but not least, high efficiency cannot be maintained throughout the whole load range.

To address deficiencies of the existing modulation schemes, we propose a novel modulation scheme. A side-by-side waveform comparison between the proposed modulation and the conventional ones is shown in Fig. 1. It can be observed in Fig. 1(b) that each half of the switching cycle incorporates a sinusoidally modulated resonant period and an intermittent period. Specifically, the intermittent period is inserted after a sinusoidal resonant cycle, rather than several or dozens of switch cycles, which is significantly different from the conventional hiccup

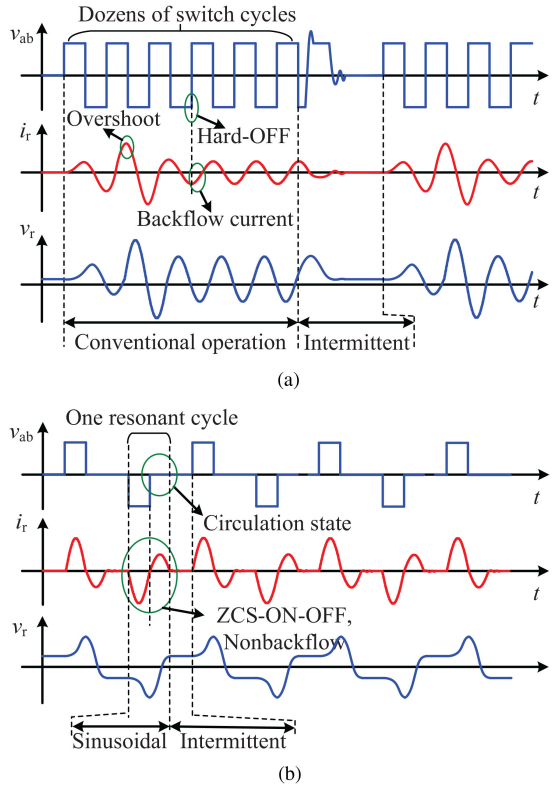

Fig. 1. Basic operating principles of the conventional and the proposed modulations. (a) Conventional modulation with hiccup mode. (b) Proposed modulation.

modulation method as shown by Fig. 1(a). Please also note that the proposed modulation is not merely segmenting the intermittent period and inserting them into each switching cycle. It also enables fully ZCS-ON/OFF, nonbackflow power, linear output characteristic, and load-independent efficiency simultaneously, which has not yet been reported in the literature. The proposed modulation can maintain high efficiency throughout the whole load range, while the reported modulation schemes suffer from efficiency deviation in the light load conditions. Therefore, the novelties and contributions of our proposed modulation are as follows:

1) linear current controllability that can ease the control and widen the output range;
2) nonbackflow power that can reduce the conduction loss;
3) fully ZCS-ON/OFF that can reduce the switching loss;
4) load-independent efficiency that enables high efficiency throughout the whole load range.

The rest of this article is organized as follows. Section II details the proposed modulation scheme and gives the mathematical description. Some performance analysis, including current controllability and fully ZCS-ON/OFF, are discussed in Section III. Section IV analyzes the power loss distribution and discusses the efficiency. A design procedure is given in Section V. Experiments are conducted in Section VI to validate the proposed modulation. Finally, Section VII concludes this article.

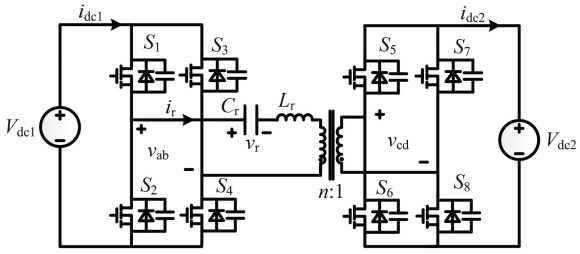

Fig. 2. Schematics of the bidirectional series resonant converter.

II. Proposed Modulation

As the schematic shown in Fig. 2, the BSRC consists of a primary full-bridge circuit and a secondary full-bridge circuit, interconnected with a series resonant tank (L_r–C_r) and a transformer. MOSFET switches S_1–S_4 in the primary full-bridge circuit are modulated to generate ac voltage v_{ab} from the dc bus V_{dc1}. The transformer with a turns ratio of $n:1$ provides an isolated step-down voltage conversion. The secondary full-bridge circuit includes MOSFET switches S_5–S_8, which are modulated to generate ac voltage v_{cd} from the dc bus V_{dc2}. The series resonant tank is insusceptible to the magnetic inductance which is sufficiently large.

Based on the power flow direction and the voltage gain, the operations of the BSRC can be classified into four possible modes as follows:

1) forward-buck mode ($V_{dc1} > nV_{dc2}$): power is delivered from V_{dc1} to V_{dc2};
2) forward-boost mode ($V_{dc1} < nV_{dc2}$): power is delivered from V_{dc1} to V_{dc2};
3) reverse-boost mode ($V_{dc1} > nV_{dc2}$): power is delivered from V_{dc2} to V_{dc1};
4) reverse-buck mode ($V_{dc1} < nV_{dc2}$): power is delivered from V_{dc2} to V_{dc1}.

Since the forward-buck and forward-boost modes are the dualities of the reverse-boost and reverse-buck modes, respectively, only the analysis of the two forward modes are given in the following. The switching patterns and waveforms of the remaining two reverse modes are dualities and, thus, not repeated.

A. Forward-Buck Mode

The switching sequences and the operating waveforms of the forward-buck mode are shown in Fig. 3. The positive half cycle and the negative half cycle are symmetrical. It can be observed that there are three typical stages within half a cycle, and their equivalent circuits are shown in Fig. 4. Detailed descriptions are as follows.

Stage 1 ($0 \le t < 0.5\,T_r$). *Charging state:* This stage begins at $t = 0$ when S_1, S_4, and S_8 are turned ON. S_5 remains ON. The equivalent circuit of the BSRC is shown in Fig. 4(a). V_{dc1} is charging V_{dc2}, just like the ON-stage of a buck converter. i_r sinusoidally rises from zero to charge the resonant tank and V_{dc2}. Sinusoidal i_r and v_r can be derived as

$$i_r = -\frac{v_{r0} - V_{dc1} + nV_{dc2}}{Z_r}\sin(\omega_r t), \text{and} \tag{1}$$

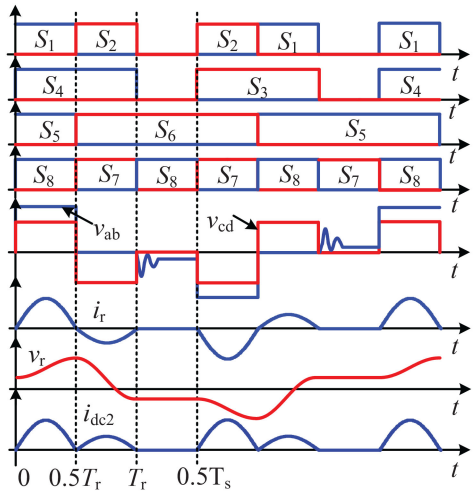

Fig. 3. Switching sequence and operating waveforms of the BSRC in forward-buck mode.

$$v_r = (v_{r0} - V_{dc1} + nV_{dc2})\cos(\omega_r t) + V_{dc1} - nV_{dc2} \tag{2}$$

where Z_r and ω_r are the characteristic impedance and the resonant angle frequency, respectively, given by

$$Z_r = \sqrt{\frac{L_r}{C_r}}, \text{and} \tag{3}$$

$$\omega_r = \frac{1}{\sqrt{L_r C_r}}. \tag{4}$$

v_{r0} is the initial value of the resonant voltage v_r.

This stage ends at $0.5T_r$ when i_r reaches zero again. T_r is the resonant period.

Stage 2 ($0.5\,T_r \le t < T_r$). *Circulating state:* At $t = 0.5T_r$, S_1, S_5, and S_8 are turned OFF, while S_2, S_6, and S_7 are ON. Since i_r is zero at $0.5T_r$, all switches realize ZCS-ON/OFF. The equal circuit is given in Fig. 4(b). v_{ab} is short-circuit, and v_{cd} is reversed as $-V_{dc2}$. The resonant tank is charging V_{dc2}, just like the OFF-stage of a buck converter. Sinusoidal i_r and v_r can be derived as

$$i_r = -\frac{v_{r1} - nV_{dc2}}{Z_r}\sin[\omega_r(t - 0.5T_r)], \text{and} \tag{5}$$

$$v_r = (v_{r1} - nV_{dc2})\cos[\omega_r(t - 0.5T_r)] + nV_{dc2} \tag{6}$$

where v_{r1} is the value of v_r at $t = 0.5T_r$.

This stage ends when i_r reaches zero again at $t = T_r$.

Stage 3 ($T_r \le t < 0.5\,T_s$). *Idle state:* After S_2, S_4, and S_7 are turned OFF at $t = T_r$, the primary bridge is open-circuit. The secondary bridge is short-circuit as S_8 is ON during this stage. The resonant tank resonates with the parasitic capacitance of switches through the transformer, as shown in Fig. 4(c). The resonant current and voltages can be derived as

$$i_r = -\frac{v_{r2}}{Z_{r1}}\sin[\omega_{r1}(t - T_r)], \tag{7}$$

$$v_r = (1 - k_1)v_{r2}\cos[\omega_{r1}(t - T_r)] + k_1 v_{r2}, \text{and} \tag{8}$$

$$v_{ab} = -k_1 v_{r2}\cos[\omega_{r1}(t - T_r)] + k_1 v_{r2}. \tag{9}$$

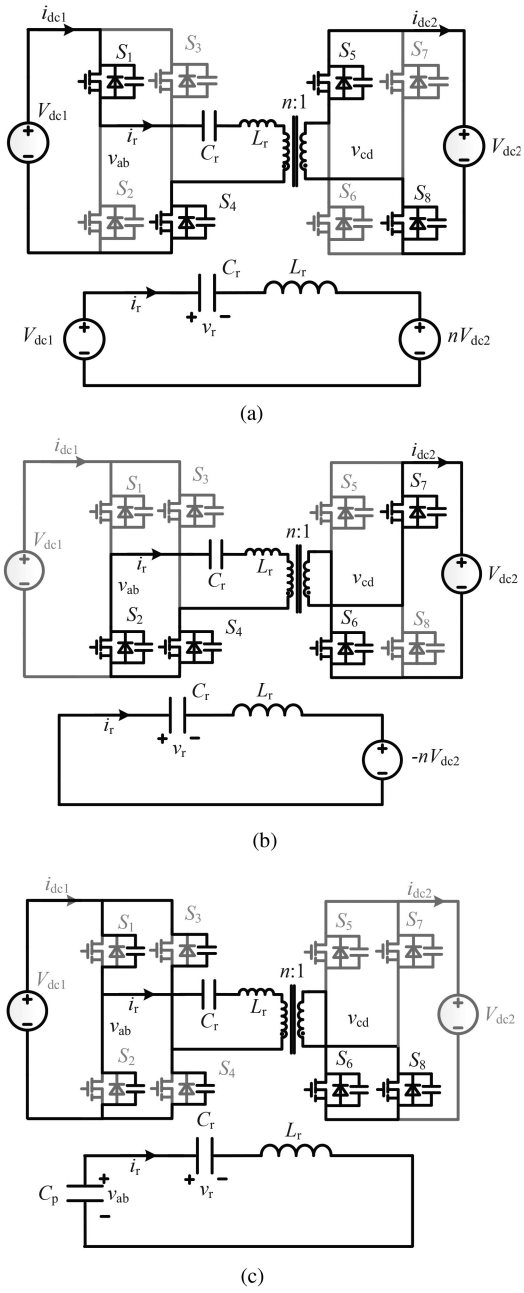

Fig. 4. Equivalent circuits in different stages for forward-buck mode. (a) *Stage 1* ($0 \le t < 0.5T_r$): charging state. (b) *Stage 2* ($0.5T_r \le t < T_r$): circulating state. (c) *Stage 3* ($T_r \le t < 0.5T_s$): idle state.

v_{r2} is the value of v_r at $t = T_r$. k_1 is defined as a coefficient given by $k_1 = \frac{C_r}{C_r + C_p}$. ω_{r1} and Z_{r1} are the resonant angular frequency and the characteristic impedance given by

$$Z_{r1} = \sqrt{\frac{L_r}{C_1}}, \text{and} \tag{10}$$

$$\omega_{r1} = \frac{1}{\sqrt{L_r C_1}} \tag{11}$$

respectively. C_1 is the equivalent resonant capacitance given by $\frac{C_r C_p}{C_r + C_p}$ and C_p is the parasitic capacitance given by $4C_{\text{ds1}}$. C_{ds1} is the junction capacitance of switches S_1–S_4.

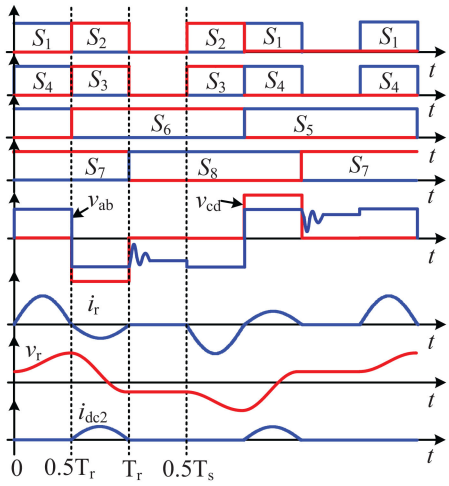

Fig. 5. Switching sequence and operating waveforms of the BSRC in forward-boost mode.

Since C_p is far smaller than C_r, k_1 is about 1, and the resonant angular frequency ω_{r1} and Z_{r1} are sufficiently large. Therefore, i_r is about zero and v_r remains v_{r2} during this stage, as shown in Fig. 3. Moreover, due to the parasitic resistance of the resonant tank and MOSFET switches, the high frequency oscillation of v_{ab} can be quickly damped and remains v_{r2}. This idle stage is maintained until $t = T_s/2$. T_s is the switching cycle.

B. Forward-Boost Mode

The switching sequences and the operating waveforms of the forward-boost mode are shown in Fig. 5, where the positive half cycle is symmetric to the negative half. There are also three typical stages within half a cycle, and their equivalent circuits are shown in Fig. 6. Detailed descriptions are as follows.

Stage 1 ($0 \le t < 0.5\,T_r$). *Circulating state:* This stage begins at $t = 0$ when S_1 and S_4 are turned ON. And S_5 and S_7 remain ON. The equivalent circuit of the BSRC is shown in Fig. 6(a). In this stage, V_{dc1} is charging the resonant tank, just like the ON-stage of a boost converter. i_r and v_r sinusoidally rise, which can be derived as

$$i_r = -\frac{v_{\text{r0}} - V_{\text{dc1}}}{Z_r} \sin(\omega_r t), \text{and} \tag{12}$$

$$v_r = (v_{\text{r0}} - V_{\text{dc1}}) \cos(\omega_r t) + V_{\text{dc1}} \tag{13}$$

respectively. The sinusoidal i_r ends at $t = 0.5T_r$.

Stage 2 ($0.5T_r \le t < T_r$). *Charging state:* At $t = 0.5T_r$, S_1, S_4, and S_5 are turned OFF, while S_2, S_3, and S_6 are turned ON. Since i_r is zero at $t = 0.5T_r$, all switches can realize ZCS-ON/OFF. The equivalent circuit is shown in Fig. 6(b). v_{ab} is reversed to $-V_{\text{dc1}}$ and v_{cd} is modulated as $-V_{\text{dc2}}$. V_{dc1} and the resonant tank are charging V_{dc2}, just like the OFF-stage of a boost converter. Sinusoidal i_r and v_r can be derived as

$$i_r = -\frac{v_{\text{r1}} + V_{\text{dc1}} - nV_{\text{dc2}}}{Z_r} \sin[\omega_r(t - 0.5T_r)], \text{and} \tag{14}$$

$$v_r = (v_{\text{r1}} + V_{\text{dc1}} - nV_{\text{dc2}}) \cos[\omega_r(t - 0.5T_r)] - V_{\text{dc1}} + nV_{\text{dc2}}. \tag{15}$$

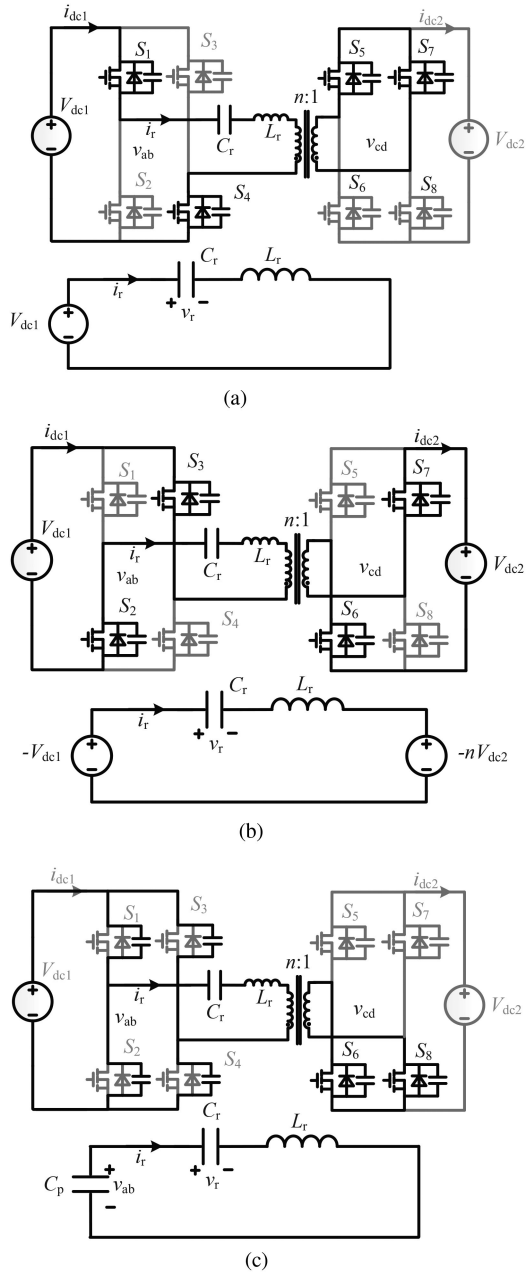

Fig. 6. Equivalent circuits in different stages for forward-boost mode. (a) *Stage 1* ($0 \le t < 0.5T_r$): circulating state. (b) *Stage 2* ($0.5T_r \le t < T_r$): charging state. (c) *Stage 3* ($T_r \le t < 0.5T_s$): idle state.

This stage ends at $t = T_r$, when i_r reaches zero again.

Stage 3 ($T_r \le t < 0.5T_s$). *Idle state:* After S_2, S_3, and S_7 are turned OFF, S_8 is turned ON at $t = T_r$, such that the primary bridge is open circuit. The resonant tank resonates with the parasitic capacitance of primary switches, as shown in Fig. 6(c). The resonant current and voltage can be derived as

$$i_r = -\frac{v_{\rm r2} + V_{\rm dc1}}{Z_{r1}} \sin[\omega_{r1}(t - T_r)], \text{and} \tag{16}$$

$$v_r = (1 - k_1)(v_{\rm r2} + V_{\rm dc1}) \cos[\omega_{r1}(t - T_r)] + k_1 v_{r2} - (1 - k_1)V_{\rm dc1}, \text{and} \tag{17}$$

$$v_{\rm ab} = -k_1(v_{\rm r2} + V_{\rm dc1}) \cos[\omega_{r1}(t - T_r)] + k_1 v_{r2} - (1 - k_1)V_{\rm dc1}. \tag{18}$$

Since the resonant capacitor C_r is large, i_r and v_r are almost kept unchanged during this stage. And the oscillation of $v_{\rm ab}$ can be quickly damped due to inner resistance. $v_{\rm ab}$ is v_{r2} at steady state. This idle stage is maintained until $t = 0.5T_s$.

Based on the above modulation scheme, sinusoidal resonant current can be generated with all switches realizing ZCS-ON/OFF. It is noteworthy that such ZCS features are independent of the load. Moreover, since the resonant current is in phase with the terminal voltage, there is no backflow power, which benefits the reduction of conduction losses. It can also be observed that T_r is determined by the inherent characteristic of the resonant tank, while T_s can be varied via control. Therefore, the output power can be readily controlled by varying T_s.

III. Performance Analysis

A. Current Controllability

1) Forward-Buck Mode: Based on the analysis in Section II, we have

$$\omega_r T_r = \pi. \tag{19}$$

According to (2) and (6), we have the following two equations for the values of v_r at $t = 0.5T_r$ and $t = T_r$

$$v_{\rm r1} = 2V_{\rm dc1} - 2nV_{\rm dc2} - v_{\rm r0}, \text{and} \tag{20}$$

$$v_{\rm r2} = 2nV_{\rm dc2} - v_{\rm r1}. \tag{21}$$

Due to the continuity and symmetry of v_r, we have the following equations for the values of v_r at $t = 0$ and $t = T_r$

$$v_{\rm r0} = -v_{\rm r2}. \tag{22}$$

By solving (20)–(22), the values of v_r can be derived as

$$v_{\rm r0} = V_{\rm dc1} - 2nV_{\rm dc2}, \text{ and} \tag{23}$$

$$v_{\rm r1} = V_{\rm dc1}, \text{and} \tag{24}$$

$$v_{\rm r2} = -V_{\rm dc1} + 2nV_{\rm dc2}. \tag{25}$$

With (1) and (23), the output power can be calculated as

$$P_o = \frac{2}{T_s} \int_0^{\frac{T_r}{2}} V_{\rm dc1} i_r dt = \frac{2nV_{\rm dc1}V_{\rm dc2}f_s}{\pi Z_r f_r}. \tag{26}$$

2) Forward-Boost Mode: Sharing similar analysis procedures of the forward-buck mode, v_r at $t = 0$, $t = 0.5T_r$, and $t = T_r$ can be derived as

$$v_{\rm r0} = 2V_{\rm dc1} - nV_{\rm dc2}, \text{and} \tag{27}$$

$$v_{\rm r1} = nV_{\rm dc2}, \text{and} \tag{28}$$

$$v_{\rm r2} = -2V_{\rm dc1} + nV_{\rm dc2} \tag{29}$$

respectively. With (14) and (28), the output power is given by

$$P_o = -\frac{2}{T_s} \int_{\frac{T_r}{2}}^{T_r} nV_{\rm dc2} i_r dt = \frac{2nV_{\rm dc1}V_{\rm dc2}f_s}{\pi Z_r f_r}. \tag{30}$$

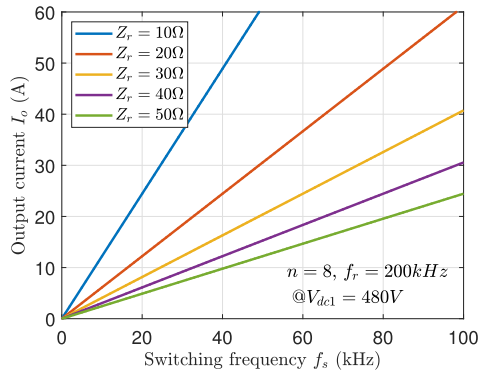

Fig. 7. Output current curves vs. switching frequency with different Z_r.

From (26) and (30), the transfer functions for the forward-buck and forward-boost modes are identical. Both share the same control variable $f_s = 1/T_s$. The BSRC can be considered as a f_s-controlled current source, as given by

$$I_o = \frac{2nV_{\rm dc1}f_s}{\pi Z_r f_r}. \tag{31}$$

Based on the analysis in Section II, the maximum switching frequency should be smaller than half-resonant frequency $\frac{f_r}{2}$. Thus, the switching frequency range is given by

$$0 < f_s \le \frac{f_r}{2}. \tag{32}$$

With (31) and (32), the output current range can be given by

$$0 < I_o \le \frac{nV_{\rm dc1}}{\pi Z_r}. \tag{33}$$

Curves of the output current I_o versus the switching frequency f_s are plotted in Fig. 7 under different designs of characteristic impedance Z_r. It is noteworthy that such linear characteristic enables simple control design.

B. Fully ZCS Range

As shown in Figs. 3 and 5, i_r is sinusoidal, which rises from zero at the beginning and falls to zero again at the end. Both full bridges shift voltage levels at zero current time realizing ZCS-ON/OFF for all switches. According to the operating principle, the constraint for ZCS-ON/OFF is that i_r should be zero at $t = 0$. It can be satisfied if and only if the converter is open circuit during the idle state. It is also known that the disconnected operation can be achieved only if the diode anode voltage is below the cathode voltage. Therefore, the constraint for ZCS-ON/OFF is given by

$$-V_{\rm dc1} \le v_{\rm r2} \le V_{\rm dc1}. \tag{34}$$

By substituting (25) and (29) into (34), the ZCS ranges are derived as

$$\frac{nV_{\rm dc2}}{V_{\rm dc1}} \le 1, \text{for forward-buck, and} \tag{35}$$

$$1 \le \frac{nV_{\rm dc2}}{V_{\rm dc1}} \le 3, \text{for forward-boost.} \tag{36}$$

Equations (35) and (36) can be satisfied via the design of the transformer turns ratio n, achieving a pretty wide voltage range. Moreover, the ZCS-ON/OFF constraint is load-independent. Fully ZCS-ON/OFF can be achieved regardless of load conditions.

Please note that "fully ZCS" means fully ZCS-ON and OFF (sinusoidal modulation) which can help in achieving high efficiency compared with conventional modulations that only realize ZVS-ON but suffer from hard switching OFF (non-ZCS-OFF) for the following three reasons.

1) The switching loss can be reduced. Commonly, conventional modulation only achieves ZVS-ON but suffers from hard switching OFF. The switching loss is up to the switch turning-OFF current $i_{\rm off}$, which could be large due to phase lag or heavy load. While the proposed modulation realize both ZCS ON and OFF simultaneously, the total switching loss is only up to the drain–source voltage $V_{\rm ds}$ and junction capacitance $C_{\rm ds}$, which is only 1 W in this article.
2) The conduction loss can be reduced. Since the proposed modulation realizes fully ZCS ON and OFF, no magnetic current is needed during the long intermittent period which is usually used to realized ZVS-ON in conventional methods, reducing the conduction loss.
3) Fully ZCS ON and OFF can be achieved over the whole load range. Commonly, the conventional modulations meet difficulties in maintaining ZVS-ON over a wide output range, especially in light load condition. Otherwise, small magnetic inductance is needed to maintain the magnetic current to realize ZVS-ON, which could result in large magnetic loss. In the proposed method, the fully ZCS ON and OFF are regardless of the load conditions.

IV. Load-Independent Efficiency

A. Loss Calculation

The power loss of the proposed BSRC can be classified into five parts in terms of the components, including *switch loss* (P_S), *transformer loss* (P_T), *inductor loss* (P_I), *capacitor loss* (P_C), and *others* (P_O). To achieve the efficiency performance, loss analysis can be conducted as follows.

1) Switch Loss: The switch loss P_S includes switching loss $P_{\rm sw.}$ and conduction loss $P_{\rm cond.}$ of switches, i.e.,

$$P_S = P_{\rm sw.} + P_{\rm cond.}. \tag{37}$$

Since ZCS-ON/OFF are realized in all the switches throughout the whole operating range, there only exists small turn-ON loss due to the parasitic capacitance of the switches. Generally, the turn-ON loss can be represented as $\frac{1}{2}C_{\rm ds}V_{\rm ds}^2 f_s$, where $C_{\rm ds}$, $V_{\rm ds}$, and f_s are the parasitic capacitance, drain–source voltage, and switching frequency, respectively. To calculate the switching loss, $v_{\rm ds}$ at the turn-ON time for each switch should be first derived based on the operating waveforms in Figs. 3 and 5. The detailed calculation process is given in Appendix A. With the calculation results of switching loss for all the switches summarized in Table III (appendix), concise expressions for $P_{\rm sw.}$ are given by (38a) and (38b) shown at the bottom of the next page.

In addition to the switching loss, the conduction loss should also be calculated. According to Figs. 3 and 5, the resonant current flows through each switch for half-switching cycle. As synchronous rectifications are realized for all switches, the overall conduction loss of all switches can be calculated by

$$P_{\text{cond.}} = I_{r,\text{rms}}^2(2r_{\text{ds1}} + 2n^2 r_{\text{ds2}}) \tag{39}$$

where r_{ds1} and r_{ds2} are drain–source resistance of the primary and secondary switches, respectively. $I_{r,\text{rms}}$ is the root mean square (rms) value of i_r, given by (40a) and (40b) shown at the bottom of this page. The detailed derivation process of (40) is given in Appendix B.

From (37) and (40), the switch loss P_S is proportional to switching frequency f_s.

2) Transformer Loss and Inductor Loss: The transformer loss P_T includes core loss $P_{T,\text{core.}}$ and conduction loss $P_{T,\text{cond.}}$, i.e.,

$$P_T = P_{T,\text{core.}} + P_{T,\text{cond.}}. \tag{41}$$

To evaluate the core loss with arbitrary magnetic flux waveforms, the generalized Steinmetz equation (GSE) [31] can be used as given by

$$P_{\text{T, core}} = V_T \frac{1}{T_s}\int_0^{T_s} k_1 \left|\frac{dB}{dt}\right|^{\alpha} |B(t)|^{\beta-\alpha} dt. \tag{42}$$

The coefficient k_1 is given by

$$k_1 = \frac{k}{(2\pi)^{\alpha-1}\int_0^{2\pi} |\cos\theta|^{\alpha} |\sin\theta|^{\beta-\alpha} d\theta} \tag{43}$$

where k, α, and β are constants determined by the magnetic material.

With the proposed modulation, the waveforms of magnetic flux density B are shown by Fig. 8. It can be observed that B is piecewise. It only varies during the sinusoidal period and keeps unchanged during the intermittent period. Such that, core loss is only incurred during the sinusoidal period. Only taking the sinusoidal period into consideration, B is triangular and can be fundamentally approximated as sinusoidal, as given by

$$B \approx \begin{cases} B_{\text{m}}\sin(\pi f_r t), & 0 \le t < T_r \\ 0, & T_r \le t < \frac{T_s}{2} \end{cases}, \text{ for buck mode} \tag{44}$$

and

$$B \approx \begin{cases} B_m, & 0 \le t < \frac{T_r}{2} \\ -B_{\text{m}}\cos(2\pi f_r t), & \frac{T_r}{2} \le t < T_r \\ -B_m, & T_r \le t < \frac{T_s}{2} \end{cases}, \text{for boost mode.} \tag{45}$$

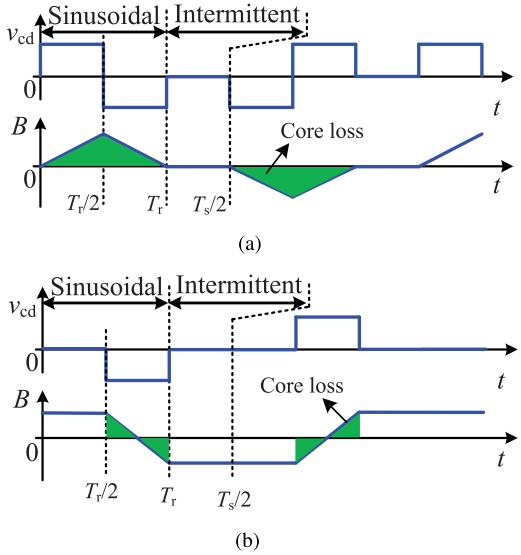

Fig. 8. Waveforms of transformer voltage and magnetic flux density. (a) Forward-buck mode. (b) Forward-boost mode.

Such that, by substituting (43), (44), and (45) into (42), the core loss can be derived as

$$P_{T,\text{core.}} = \begin{cases} V_T k(\frac{f_r}{2})^{\alpha} B_m^{\beta} \frac{2f_s}{f_r}, & \text{for buck mode} \\ V_T k(f_r)^{\alpha} B_m^{\beta} \frac{f_s}{f_r}, & \text{for boost mode} \end{cases}. \tag{46}$$

It can be found in (46) that the core loss of the proposed method is linearly varying with the switching frequency.

The conduction loss of the transformer $P_{T,\text{cond.}}$ is decided by $I_{r,\text{rms}}$ and the transformer wire ac resistor $r_{\text{AC,T}}$, as given by

$$P_{\text{T,cond.}} = I_{r,\text{rms}}^2 r_{\text{AC,T}}. \tag{47}$$

$r_{\text{AC,T}}$ can be measured by an inductance capacitance resistance (LCR) meter. Please note that the resonant current does not vary at the switching frequency due to the insertion of intermittent period within the switching cycle. In fact, the resonant current varies at fixed half-resonant frequency $0.5f_r$, which can be observed from the switching sequence and operating waveforms in Figs. 3 and 5. The measurement is at fixed frequency, regardless of the variable switching frequency.

The inductor loss P_I also includes core loss $P_{I,\text{core.}}$ and the conduction loss $P_{I,\text{cond.}}$. The calculation is the same as that of the transformer, and thus not repeated for conciseness.

From (46) and (47), the transformer and inductor losses are also proportional to f_s.

$$P_{\text{sw.}} = \begin{cases} (C_{\text{ds1}}V_{\text{dc1}}^2 + 4C_{\text{ds2}}V_{\text{dc2}}^2 + 2C_{\text{ds1}}n^2V_{\text{dc2}}^2)f_s, & \text{for forward-buck} \quad (38a) \\ 2[C_{\text{ds1}}V_{\text{dc1}}^2 + C_{\text{ds2}}V_{\text{dc2}}^2 + \frac{C_{\text{ds1}}}{4}(nV_{\text{dc2}} - V_{\text{dc1}})^2]f_s, & \text{for forward-boost} \quad (38b) \end{cases}$$

$$I_{r,\text{rms}} = \begin{cases} \frac{1}{Z_r}\sqrt{\frac{f_s}{2f_r}[(nV_{\text{dc2}})^2 + (V_{\text{dc1}} - nV_{\text{dc2}})^2]}, & \text{for forward-buck} \quad (40a) \\ \frac{1}{Z_r}\sqrt{\frac{f_s}{2f_r}[(V_{\text{dc1}})^2 + (V_{\text{dc1}} - nV_{\text{dc2}})^2]}, & \text{for forward-boost} \quad (40b) \end{cases}$$

3) Capacitor Loss and Other Loss: The capacitor loss P_C is caused by the equivalent series resistance (ESR) of the resonant capacitor, as given by

$$P_C = I_{r,\mathrm{rms}}^2 r_{\mathrm{Cap}} \tag{48}$$

where r_{Cap} represents ESR of the capacitor and can be obtained from the datasheet.

The other loss P_O is caused by the wire resistance and contact resistance of the circuit. The resistance can be represented by r_O that can also be measured by an LCR meter. Such that, the other loss can be evaluated as

$$P_O = I_{r,\mathrm{rms}}^2 r_O. \tag{49}$$

With (40), the capacitor loss P_C and other loss P_O are proportional to switching frequency f_s as well.

B. Efficiency Analysis

Based on the above analysis, the total power loss of the proposed BSRC is given by

$$P_{\mathrm{Loss}} = P_S + P_T + P_I + P_C + P_O. \tag{50}$$

With (37)–(49), each component loss in (50) is proportional to switching frequency f_s. Thus, the total power loss can be represented as a function of f_s given by

$$P_{\mathrm{Loss}} = p_1 f_s \tag{51}$$

where p_1 is defined as a loss coefficient and can be calculated according to (37)–(49).

Moreover, as analyzed in Section III-A, the output power is also a function of f_s. Similarly, an output power coefficient p_2 can be defined. p_2 can be calculated with (26) and (30). The output power can be represented by

$$P_o = p_2 f_s. \tag{52}$$

Thus, the efficiency of the BSRC with the proposed modulation scheme is given by

$$\eta = \frac{P_o}{P_o + P_{\mathrm{Loss}}} = \frac{p_2}{p_1 + p_2}. \tag{53}$$

The efficiency is independent of the load condition, and, thus, the high efficiency performance maintains throughout the whole load range.

V. Design Procedure

With the linear output characteristic, the BSRC is ready to design against wide-range input and output. Given input voltage $V_{\mathrm{dc1}} \in [V_{\mathrm{dc1,\,min}}, V_{\mathrm{dc1,\,max}}]$, output voltage $V_{\mathrm{dc2}} \in [V_{\mathrm{dc2,\,min}}, V_{\mathrm{dc2,\,max}}]$, output current $I_{\mathrm{o}} \in (0, I_{\mathrm{o,\,max}}]$, and switching frequency range $f_s \in (0,\ f_{\mathrm{s,max}}]$, a five-step procedure can be taken to design the transformer and the resonant tank as follows.

1) *Step 1:* Choose the resonant frequency f_r. Since the switching frequency f_s should be below half of the resonant frequency, i.e., $0.5 f_r$, f_r can be given by

$$f_r \geq 2 f_{s,\max}. \tag{54}$$

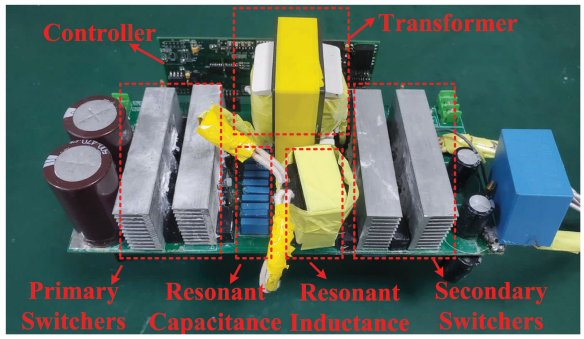

Fig. 9. Photograph of the experiment prototype.

2) *Step 2:* Determine the turns ratio n of the transformer. To realize ZCS-ON/OFF against the wide-range specifications, according to the conditions of fully ZCS in (35) and (36), n should meet the equation given by

$$n \leq \frac{3V_{\mathrm{dc1,\,min}}}{V_{\mathrm{dc2,\,max}}}. \tag{55}$$

3) *Step 3:* Design the primary and secondary turn numbers N_1 and N_2 of the transformer. As the maximum magnetic flux density B_m is given by

$$B_m = \begin{cases} \frac{V_{\mathrm{dc2}}}{2 f_r N_2 A_e}, & \text{for forward-buck} \\ \frac{V_{\mathrm{dc2}}}{4 f_r N_2 A_e}, & \text{for forward-boost} \end{cases} \tag{56}$$

where A_e is the core's effective flux cross-sectional area. Since B_m reaches the maximum value in forward-buck mode, N_2 and N_1 can be designed as

$$N_2 = \frac{V_{\mathrm{dc2,max}}}{2 f_r B_m A_e}, \text{ and} \tag{57}$$

$$N_1 = n N_2. \tag{58}$$

4) *Step 4:* Calculate the characteristic impedance Z_r. According to the power features in Section III-A, Z_r can be calculated to obtain the maximum output current, as given by

$$Z_r \leq \frac{2 n V_{\mathrm{dc1,min}} f_{s,\max}}{\pi I_{o,\,\max} f_r}. \tag{59}$$

5) *Step 5:* Design the resonant tank. With the calculated f_r and Z_r, the resonant tank parameters can be designed as

$$L_r \leq \frac{n V_{\mathrm{dc1,min}} f_{s,\max}}{\pi^2 f_r^2 I_{o,\,\max}} \tag{60}$$

$$C_r \geq \frac{I_{o,\,\max}}{4 n V_{\mathrm{dc1,min}} f_{s,\max}}. \tag{61}$$

VI. Experimental Verification

To verify the aforementioned characteristics achieved by the proposed modulation, a 1-kVA BSRC prototype is built with specifications and parameters given in Table I. The photograph of the experiment prototype is shown in Fig. 9. A power analyzer modeled HIOKI 3390 is used to measure the system efficiency.

TABLE I
SPECIFICATIONS AND PARAMETERS OF THE BSRC

Specifications		Symbols	Values
Primary side	Voltage range	$V_{\mathrm{dc}\,1}$	240–480 V
	Current range	$I_{\mathrm{dc}\,1}$	0–5 A
Secondary side	Voltage range	$V_{\mathrm{dc}\,2}$	48 V
	Current range	$I_{\mathrm{dc}\,2}$	0–20 A

Parameters	Symbols	Values
Primary-side switches	S_1 – S_4	E3M0065090D
Secondary-side switches	S_5 – S_8	E3MIPP030N10N5D
Resonant inductor	L_r	20 μH
Resonant capacitor	C_r	31 nF, B32652A2102J000
Resonant frequency	f_r	200 kHz
Switching frequency	f_s	2–100 kHz
Turns ratio	n	8:1
Transformer		EE65/32/27 PC95
Inductor		EE42/21/20 PC95
Controller		TMS320F28335
Driver		SI8233

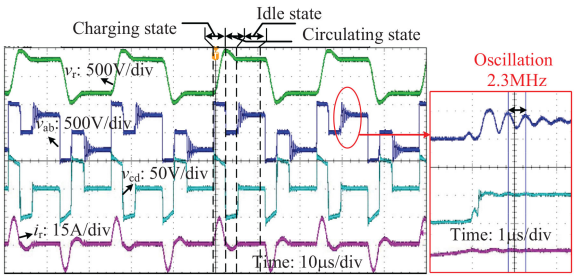

Fig. 10. Operation waveforms of the BSRC for forward-buck mode.

The turns ratio of the transformer is 8:1. The input voltage varies from 240 to 480 V, while the output voltage is fixed at 48 V. Thus, the BSRC works at both forward-buck and forward-boost modes. The reverse modes are dualities of the forward modes and, thus, not presented here for concise.

A. Operating Waveforms, Fully ZCS, and Current Controllability

The operating waveforms of the forward-buck mode are captured in Fig. 10. The input voltage is 480 V and the output voltage is 48 V. v_{ab}, v_{cd}, v_r, and i_r are consistent with the operating principle of the forward-buck mode analyzed in Section II-A and shown in Fig. 10. In the charging state, v_{ab} and v_{cd} are both positive. In the circulating state, v_{ab} and v_{cd} are zero and negative, respectively. In the idle state, v_{cd} is zero, while v_{ab} first resonates with primary switches' parasitic capacitance but is quickly damped.

It can be observed that i_r is sinusoidal and in phase with v_{cd} as well as v_{ab}. Thus, there is no backflow power. The ZCS behaviors of S_1, S_3, S_5, and S_7 are depicted in Fig. 11. The switching waveforms of S_2, S_4, S_6, and S_8 are similar. The switches turn ON and OFF when the current is close to zero realizing ZCS-ON/OFF simultaneously.

The operating waveforms of the forward-boost mode are captured in Fig. 12. The input voltage is 240 V and the output voltage is 48 V. v_{ab}, v_{cd}, v_r, and i_r are consistent with the operating principle for the forward-boost mode analysis analyzed in Section II-B and shown in Fig. 12. In circulating state, v_{ab} and v_{cd} are positive and zero, respectively. In the charging state, v_{ab} and v_{cd} are both negative. In the idle state, v_{cd} is still zero, while v_{ab} is open resonating with primary switches' parasitic capacitance. Nonbackflow power exits. The ZCS behaviors of S_1, S_3, S_5, and S_7 are depicted in Fig. 13(a)–(d). The switching

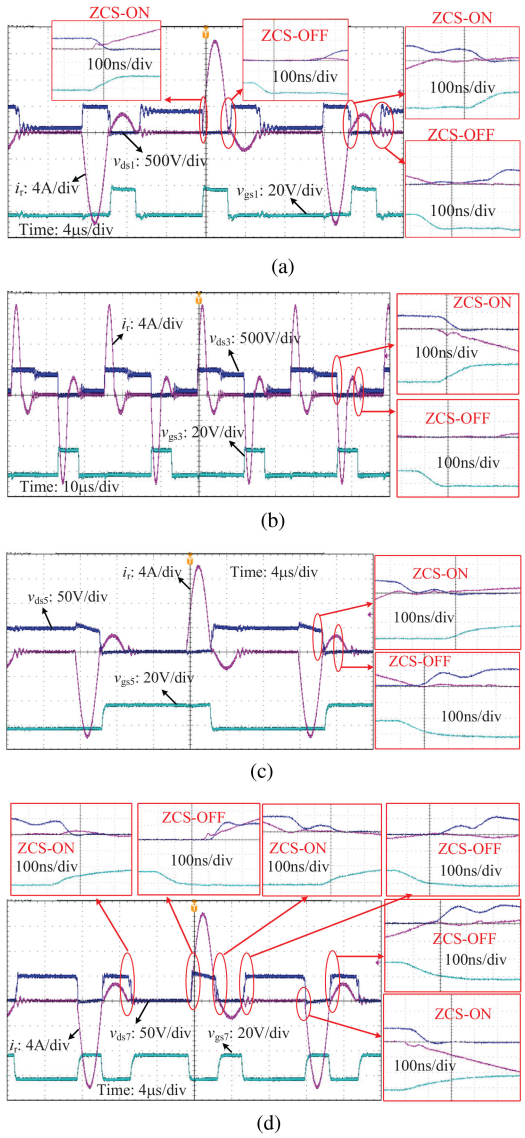

Fig. 11. ZCS-ON/OFF waveforms of the BSRC for forward-buck mode. (a) ZCS-ON/OFF waveforms of S_1. (b) ZCS-ON/OFF waveforms of S_3. (c) ZCS-ON/OFF waveforms of S_5. (d) ZCS-ON/OFF waveforms of S_7.

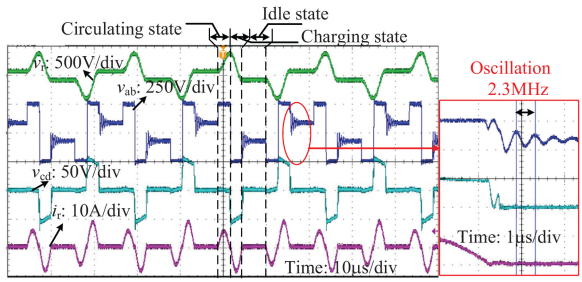

Fig. 12. Operation waveforms of the BSRC for forward-boost mode.

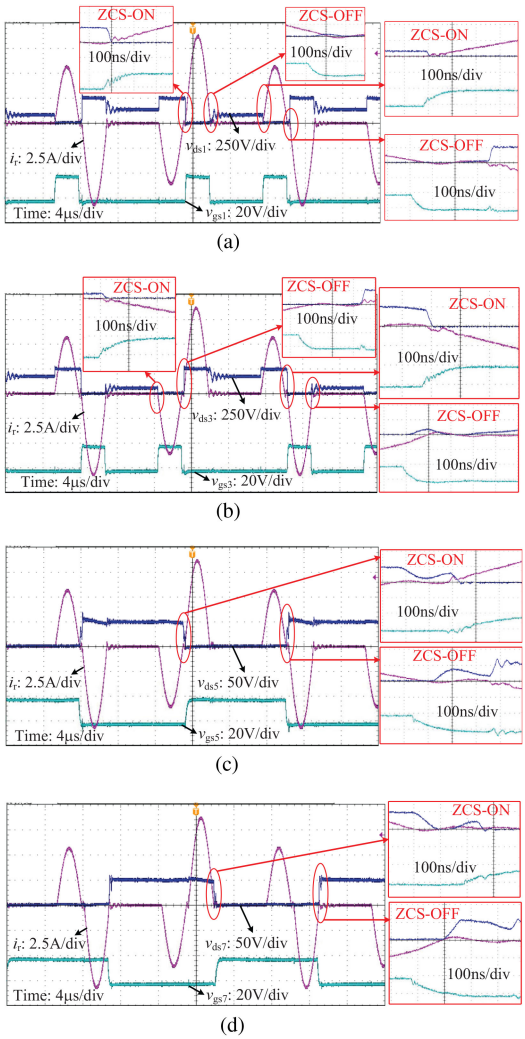

Fig. 13. ZCS-ON/OFF waveforms of the BSRC for forward-boost mode. (a) ZCS-ON/OFF waveforms of S_1. (b) ZCS-ON/OFF waveforms of S_3. (c) ZCS-ON/OFF waveforms of S_5. (d) ZCS-ON/OFF waveforms of S_7.

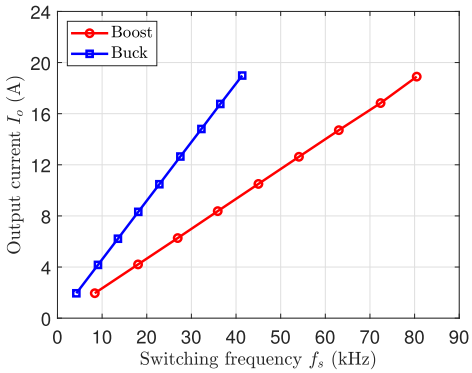

Fig. 14. Measured current versus switching frequency with $V_{\rm dc2} = 48$ V.

waveforms of S_2, S_4, S_6, and S_8 are similar. All switches turn ON and OFF when the current is close to zero realizing ZCS-ON/OFF simultaneously.

The output current versus the switching frequency are measured, as shown in Fig. 14. The output power linearly increases with the switching frequency for both forward-buck ($V_{\rm dc1} = 480$ V) and forward-boost ($V_{\rm dc1} = 240$ V) modes.

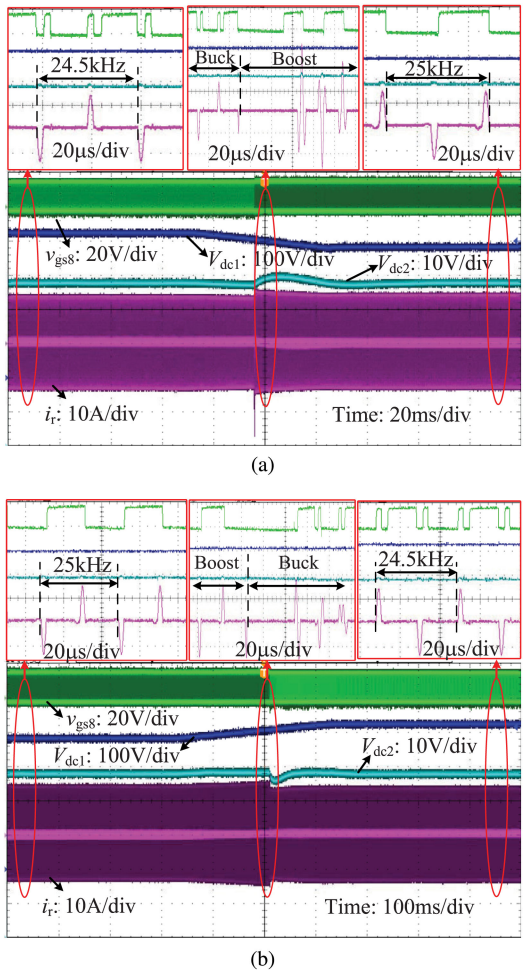

Fig. 15. Transition waveforms between forward-buck and forward-boost mode of the BSRC with $V_{\rm dc2} = 48$ V. (a) Transition waveform from $V_{\rm dc1} = 420$ to 380 V. (b) Transition waveform from $V_{\rm dc1} = 380$ to 420 V.

B. Transient Waveforms

Fig. 15(a) shows the transient waveforms when the forward-buck mode is changed to forward-boost mode. The output voltage is regulated to 48 V with the load resistance being 5 Ω. First, the input voltage is set at 420 V. The BSRC works in the forward-buck mode with switching frequency being 24.5 kHz. Then, the input voltage begins to fall toward 380 V within 50 ms. When the input voltage is 400 V, the work mode is changed to forward-boost. In the steady-state of the forward-boost mode, the switching frequency is 25 kHz. It can be observed that the output voltage can be tightly regulated.

Similarly, Fig. 15(b) shows the transient waveforms from the forward-boost to forward-buck mode. At first, the input voltage is 380 V and the converter works at forward-boost mode with a switching frequency of 25 kHz. Then the input voltage rises to 420 V within 300 ms. The switching frequency falls with the increase of input voltage. When the input voltage is 400 V, the work mode is changed to forward-buck, decreasing the

TABLE II
QUANTITATIVE AND QUALITATIVE REVIEW OF BIDIRECTIONAL DC/DC CONVERTERS

Methodology	Power(W)	Efficiency @Light Load	Efficiency @Full Load	Reasons for efficiency degradation		Output
				Backflow power	Switching	
Optimal Design [7]	100-1000	84%	96%	Exits	ZVS-ON, hard-OFF	nonlinear
Multi-Resonant Tank [32]	1000	90%	96%	Exits	ZVS-ON, hard-OFF	nonlinear
Multi-Topology [33]	80-400	80%	94%	Exits	ZVS-ON, hard-OFF	nonlinear
Optimizing Control [18]	20-200	70%	91%	Exits	ZVS-ON, hard-OFF	nonlinear
Optimizing Control and Topology [34]	100-500	80%	92%	Exits	ZVS-ON, hard-OFF	nonlinear
Intermittent Sinusoidal(Proposed Modulation)	100-900	95%	96%	None	ZCS-ON, ZCS-OFF	linear

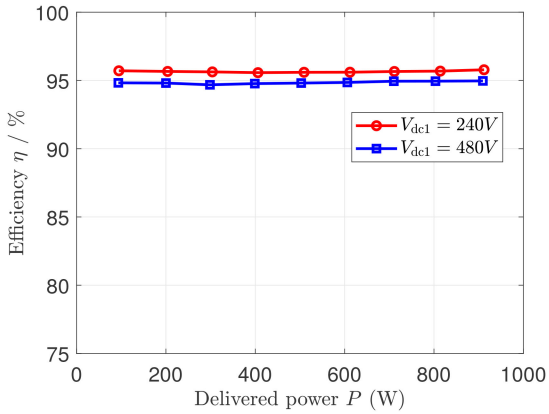

Fig. 16. Measured efficiency versus power with $V_{dc2} = 48$ V.

output voltage. Then switching frequency is regulated to rise to 24.5 kHz at the steady-state.

Smooth transition can be achieved between the forward-buck mode and forward-boost mode.

C. Measured Efficiency

The measured efficiency versus the delivered power is plotted in Fig. 16. The blue line and red line indicate the efficiency curves of the forward-buck mode ($V_{dc1} = 480$ V) and forward-boost mode ($V_{dc1} = 240$ V), respectively. The output power ranges from 100 to 900 W. It can be observed that the efficiencies are almost constant at 95% and 95.8% for the forward-buck mode and forward-boost mode, respectively, regardless of the load power.

Fig. 17 also depicts the power loss breakdown. It can be observed that all loss components are nearly proportional to the output power, and, thus, the efficiency performance is independent of the load. Moreover, the switching loss only has a very small proportion, due to the fully ZCS-ON/OFF.

D. Comparison With the State-of-the-Art Works

Table II gives a comparison between the proposed work and some state-of-the-art works from both quantitative and qualitative aspects. It can be observed that existing modulation schemes typically suffer from significant efficiency degradation, i.e., several to dozens of percentages, in light load conditions. The reasons for efficiency degradation mainly include backflow power and hard switching-OFF. These issues are successfully addressed by the proposed method, such that high efficiency

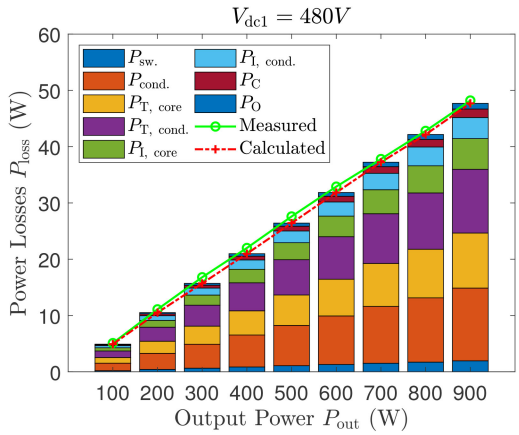

(a)

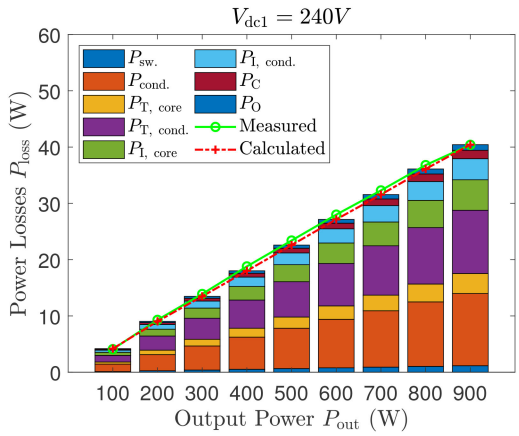

(b)

Fig. 17. Power loss breakdown for forward-buck and forward-boost modes. (a) Loss breakdown for $V_{dc1} = 480$ V and $V_{dc2} = 48$ V. (b) Loss breakdown for $V_{dc1} = 240$ V and $V_{dc2} = 48$ V.

can be maintained throughout the whole load range, from 95% to 96%. Moreover, linear output characteristic can also be achieved to ease the control.

VII. CONCLUSION

In this article, a novel intermittent sinusoidal modulation is proposed for BSRC achieving fully ZCS-ON/OFF, current controllability, and high load-independent efficiency. Compared with conventional sinusoidal modulation, wide-range regulation can be achieved by incorporating an intermittent period and a resonant period into a switching cycle. ZCS-ON/OFF can be achieved for all switches with the proposed modulation scheme.

TABLE III
SWITCHING LOSS OF EACH SWITCH

Mode	Switch	$t=0$	$t=0.5T_r$	$t=T_r$	$t=0.5T_s$	$t=0.5T_s+0.5T_r)$	$t=0.5T_s+T_r)$	Switching Loss
Forward-buck	S_1	$nV_{\rm dc2}$	–	–	–	$V_{\rm dc1}$	–	$0.5C_{\rm ds1}(V_{\rm dc1}^2+n^2V_{\rm dc2}^2)f_s$
	S_2	–	$V_{\rm dc1}$	–	$nV_{\rm dc2}$	–	–	$0.5C_{\rm ds1}(V_{\rm dc1}^2+n^2V_{\rm dc2}^2)f_s$
	S_3	–	–	–	$nV_{\rm dc2}$	–	–	$0.5C_{\rm ds1}n^2V_{\rm dc2}^2f_s$
	S_4	$nV_{\rm dc2}$	–	–	–	–	–	$0.5C_{\rm ds1}n^2V_{\rm dc2}^2f_s$
	S_5	–	–	–	–	$V_{\rm dc2}$	–	$0.5C_{\rm ds2}V_{\rm dc2}^2f_s$
	S_6	–	$V_{\rm dc2}-$	–	–	–	–	$0.5C_{\rm ds2}V_{\rm dc2}^2f_s$
	S_7	–	$V_{\rm dc2}$	–	$V_{\rm dc2}$	–	$V_{\rm dc2}$	$1.5C_{\rm ds2}V_{\rm dc2}^2f_s$
	S_8	$V_{\rm dc2}$	–	$V_{\rm dc2}$	–	$V_{\rm dc2}$	–	$1.5C_{\rm ds2}V_{\rm dc2}^2f_s$
Forward-boost	S_1	$0.5(nV_{\rm dc2}-V_{\rm dc1})$	–	–	–	$V_{\rm dc1}$	–	$0.5C_{\rm ds1}[0.25(nV_{\rm dc2}-V_{\rm dc1})^2+V_{\rm dc1}^2]f_s$
	S_2	–	$V_{\rm dc1}$	–	–	$nV_{\rm dc2}-V_{\rm dc1}$	–	$0.5C_{\rm ds1}[0.25(nV_{\rm dc2}-V_{\rm dc1})^2+V_{\rm dc1}^2]f_s$
	S_3	–	$V_{\rm dc1}$	–	–	$nV_{\rm dc2}-V_{\rm dc1}$	–	$0.5C_{\rm ds1}[0.25(nV_{\rm dc2}-V_{\rm dc1})^2+V_{\rm dc1}^2]f_s$
	S_4	$0.5(nV_{\rm dc2}-V_{\rm dc1})$	–	–	–	$V_{\rm dc1}$	–	$0.5C_{\rm ds1}[0.25(nV_{\rm dc2}-V_{\rm dc1})^2+V_{\rm dc1}^2]f_s$
	S_5	–	–	–	–	$V_{\rm dc2}$	–	$0.5C_{\rm ds2}V_{\rm dc2}^2f_s$
	S_6	-	$V_{\rm dc2}$	–	–	–	–	$0.5C_{\rm ds2}V_{\rm dc2}^2f_s$
	S_7	–	–	–	–	–	$V_{\rm dc2}$	$0.5C_{\rm ds2}V_{\rm dc2}^2f_s$
	S_8	–	–	$V_{\rm dc2}$	–	–	–	$0.5C_{\rm ds2}V_{\rm dc2}^2f_s$

The output characteristic of the BSRC behaves as a switching frequency dependent current source that meets the requirement of a wide-range voltage gain. Moreover, the power loss linearly rises with the switching frequency obtaining a load-independent efficiency. High efficiency can be achieved for the whole operating range.

APPENDIX

A. Calculation of Switching Loss

Based on the operating waveforms in Figs. 3 and 5, values of $V_{\rm ds}$ at the turn-ON time for each switch are different in forward-buck and forward-boost modes. Nevertheless, all the switches share a similar calculation process. Here, we first take the switching loss calculation of S_2 in the forward-buck mode as an example, and then summarize all the results for the other switches in Table III.

As shown in Fig. 3, S_2 turns ON at $t=0.5T_r$ and $t=0.5T_s$ within a switching cycle. The turn-ON loss of S_2 can be calculated by

$$P_{\rm ON,\,S_2}=\frac{1}{2}C_{\rm ds1}(V_{\rm ds,S_2,0.5T_r}^2+V_{\rm ds,S_2,0.5T_s}^2)f_s \tag{A1}$$

where $V_{\rm ds,S_2,0.5T_r}$ and $V_{\rm ds,S_2,0.5T_s}$ are the drain–source voltage values of S_2 at $t=0.5T_r$ and $t=0.5T_s$, respectively, and $C_{\rm ds1}$ is the junction capacitance of S_1–S_4.

As shown in Fig. 3, S_1 and S_4 are ON before $t=0.5T_r$, and then

$$V_{\rm ds,S_2,0.5T_r}=V_{\rm dc1}. \tag{A2}$$

S_1–S_4 are all OFF before $t=0.5T_s$. $v_{\rm ab}$ is equal to the resonant voltage v_{r2}, given by (25). Such that

$$v_{\rm ab}=V_{\rm ds,\,S_2}-V_{\rm ds,\,S_4}=V_{\rm ds,\,S_3}-V_{\rm ds,\,S_1} \tag{A3}$$

where $V_{\rm ds,\,S_1}$–$V_{\rm ds,\,S_4}$ are the drain–source voltages of S_1–S_4, respectively. The bridge voltage is clamped by the input voltage; thus

$$V_{\rm dc1}=V_{\rm ds,\,S_1}+V_{\rm ds,\,S_2}=V_{\rm ds,\,S_3}+V_{\rm ds,\,S_4}. \tag{A4}$$

Moreover, due to the symmetry and continuity of the circuit, the drain–source voltage of S_1 and S_2 should be identical to S_4 and S_3, respectively, given by

$$V_{\rm ds,S_1}=V_{\rm ds,S_4},\,\text{and} \tag{A5}$$

$$V_{\rm ds,S_2}=V_{\rm ds,S_3}. \tag{A6}$$

With (A3)–(A6), the drain–source voltages of S_1–S_4 can be derived as

$$V_{\rm ds,S_1}=V_{\rm ds,S_4}=\frac{V_{\rm dc2}-v_{\rm ab}}{2},\,\text{and} \tag{A7}$$

$$V_{\rm ds,S_2}=V_{\rm ds,S_3}=\frac{V_{\rm dc2}+v_{\rm ab}}{2}. \tag{A8}$$

Therefore, $V_{\rm ds,S_2,0.5T_s}$ can be derived as

$$V_{\rm ds,S_2,0.5T_s}=nV_{\rm dc2}. \tag{A9}$$

With (A1), (A2), and (A9), the switching loss of S_2, donated by $P_{\rm sw.,S2}$, can be calculated by

$$P_{\rm sw.,S2}=\frac{1}{2}C_{\rm ds1}(V_{\rm dc1}^2+n^2V_{\rm dc2}^2)f_s. \tag{A10}$$

Similar calculation procedures can be applied in the calculation of switching losses for the other switches. The results are summarized in Table III.

B. Calculation of $I_{r,\mathrm{rms}}$

According to Section III-A, i_r during half-switching cycle in forward-buck mode can be described as

$$i_r = \begin{cases} \frac{nV_{\mathrm{dc2}}}{Z_r}\sin(\omega_r t), & 0 \le t < \frac{T_r}{2} \\ \frac{nV_{\mathrm{dc2}}-V_{\mathrm{dc1}}}{Z_r}\sin[\omega_r(t-\frac{T_r}{2})], & \frac{T_r}{2} \le t < T_r \\ 0. & T_r \le t < \frac{T_s}{2} \end{cases}. \quad \text{(A11)}$$

Then the rms value of i_r in forward-buck mode can be derived as

$$I_{r,\mathrm{rms}} = \frac{1}{Z_r}\sqrt{\frac{f_s}{2f_r}[(nV_{\mathrm{dc2}})^2 + (V_{\mathrm{dc1}} - nV_{\mathrm{dc2}})^2]}. \quad \text{(A12)}$$

Similarly, i_r during half-switching cycle in forward-boost mode can be derived as

$$i_r = \begin{cases} \frac{nV_{\mathrm{dc2}}-V_{\mathrm{dc1}}}{Z_r}\sin(\omega_r t), & 0 \le t < \frac{T_r}{2} \\ \frac{-V_{\mathrm{dc1}}}{Z_r}\sin[\omega_r(t-\frac{T_r}{2})], & \frac{T_r}{2} \le t < T_r \\ 0. & T_r \le t < \frac{T_s}{2} \end{cases}. \quad \text{(A13)}$$

The rms value of i_r in forward-boost mode is given as

$$I_{r,\mathrm{rms}} = \frac{1}{Z_r}\sqrt{\frac{f_s}{2f_r}[(V_{\mathrm{dc1}})^2 + (V_{\mathrm{dc1}} - nV_{\mathrm{dc2}})^2]}. \quad \text{(A14)}$$

REFERENCES

[1] G. Wang *et al.*, "A review of power electronics for grid connection of utility-scale battery energy storage systems," *IEEE Trans. Sustain. Energy*, vol. 7, no. 4, pp. 1778–1790, Oct. 2016.

[2] S. Dey, Y. Shi, K. Smith, A. M. Colclasure, and X. Li, "From battery cell to electrodes: Real-time estimation of charge and health of individual battery electrodes," *IEEE Trans. Ind. Electron.*, vol. 67, no. 3, pp. 2167–2175, Mar. 2020.

[3] D. Li, Z. Zhang, P. Liu, Z. Wang, and L. Zhang, "Fault diagnosis of battery systems for electric vehicles based on voltage abnormality combining the long short-term memory neural network and the equivalent circuit model," *IEEE Trans. Power Electron.*, vol. 36, no. 2, pp. 1303–1315, Feb. 2021.

[4] D. Bourner, "Bidirectional DC-DC converter systems: Sustaining power component design methodology to achieve critical power conditioning," *IEEE Power Electron. Mag.*, vol. 5, no. 2, pp. 66–71, Jun. 2018.

[5] X. Pan, H. Li, T. Zhao, C. Ju, and A. K. Rathore, "An overview and comprehensive comparative evaluation of current-fed-isolated-bidirectional DC-DC converter," *IEEE Trans. Power Electron.*, vol. 35, no. 3, pp. 2737–2763, Mar. 2020.

[6] B. Saha and K. Goebel, "Battery data set," NASA Ames Prognostics Data Repository, 2007. [Online]. Available: https://ti.arc.nasa.gov/tech/dash/groups/pcoe/prognostic-data-repository/#battery

[7] W. Chen, P. Rong, and Z. Lu, "Snubberless bidirectional DC-DC converter with new CLLC resonant tank featuring minimized switching loss," *IEEE Trans. Ind. Electron.*, vol. 57, no. 9, pp. 3075–3086, Sep. 2010.

[8] W. L. Malan, D. M. Vilathgamuwa, and G. R. Walker, "Modeling and control of a resonant dual active bridge with a tuned CLLC network," *IEEE Trans. Power Electron.*, vol. 31, no. 10, pp. 7297–7310, Oct. 2016.

[9] P. He, A. Mallik, A. Sankar, and A. Khaligh, "Design of a 1-MHz high-efficiency high-power-density bidirectional GaN-based CLLC converter for electric vehicles," *IEEE Trans. Veh. Technol.*, vol. 68, no. 1, pp. 213–223, Apr. 2019.

[10] C. O. Yeon, K. Jong-Woo, P. Moo-Hyun, J. Yu-Jin, L. Cheon-Yong, and G. W. Moon, "Bode plot and impedance asymptotes for light-load regulation of LLC series resonant converter," in *Proc. 8th Annu. IEEE Int. Power Electron. Motion Control Conf.*, Hefei, China, 2016, pp. 3191–3197.

[11] Z. Fang *et al.*, "Energy feedback control of light-load voltage regulation for LLC resonant converter," *IEEE Trans. Power Electron.*, vol. 34, no. 5, pp. 4807–4819, May 2019.

[12] X. Li and A. K. S. Bhat, "Analysis and design of high-frequency isolated dual-bridge series resonant DC-DC converter," *IEEE Trans. Power Electron.*, vol. 25, no. 4, pp. 850–862, Apr. 2010.

[13] R. W. DeDoncker, D. M. Divan, and M. H. Kheraluwala, "A three-phase soft-switched high-power-density DC-DC converter for high-power applications," *IEEE Trans. Ind. Appl.*, vol. 27, no. 1, pp. 63–73, Jan./Feb. 1991.

[14] L. Corradini, D. Seltzer, D. Bloomquist, R. Zane, D. Maksimovic, and B. Jacobson, "Minimum current operation of bidirectional dual-bridge series resonant DC-DC converters," *IEEE Trans. Power Electron.*, vol. 27, no. 7, pp. 3266–3276, Jul. 2012.

[15] F. Bez, W. Han, and L. Corradini, "A low-complexity trajectory controller for reduced conduction losses in series-resonant dual half-bridge converters," *IEEE Trans. Power Electron.*, vol. 33, no. 11, pp. 9963–9974, Nov. 2018.

[16] S. Hu, X. Li, and A. K. S. Bhat, "Operation of a bidirectional series-resonant converter with minimized tank current and wide ZVS range," *IEEE Trans. Power Electron.*, vol. 34, no. 1, pp. 904–915, Jan. 2019.

[17] C. Bai, B. Han, B. Kwon, and M. Kim, "High efficiency bidirectional series-resonant DC/DC converter over wide range of battery voltage," *IEEE Trans. Power Electron.*, vol. 35, no. 4, pp. 3636–3650, Apr. 2020.

[18] T. Zhu, F. Zhuo, F. Zhao, F. Wang, H. Yi, and T. Zhao, "Optimization of extended phase-shift control for full-bridge CLLC resonant converter with improved light-load efficiency," *IEEE Trans. Power Electron.*, vol. 35, no. 10, pp. 11129–11142, Oct. 2020.

[19] F. Krismer and J. W. Kolar, "Closed form solution for minimum conduction loss modulation of DAB converters," *IEEE Trans. Power Electron.*, vol. 27, no. 1, pp. 174–188, Jan. 2012.

[20] S. Shao, M. Jiang, W. Ye, Y. Li, J. Zhang, and K. Sheng, "Optimal phase-shift control to minimize reactive power for a dual active bridge DC-DC converter," *IEEE Trans. Power Electron.*, vol. 34, no. 10, pp. 10193–10205, Oct. 2019.

[21] W. Han and L. Corradini, "Wide-range ZVS control technique for bidirectional dual-bridge series resonant DC-DC converters," *IEEE Trans. Power Electron.*, vol. 34, no. 10, pp. 10256–10269, Oct. 2019.

[22] W. Han and L. Corradini, "General closed-form ZVS analysis of dual-bridge series resonant DC-DC converters," *IEEE Trans. Power Electron.*, vol. 34, no. 9, pp. 9289–9302, Sep. 2019.

[23] M. Yaqoob, K. H. Loo, and Y. M. Lai, "A four-degrees-of-freedom modulation strategy for dual-active-bridge series-resonant converter designed for total loss minimization," *IEEE Trans. Power Electron.*, vol. 34, no. 2, pp. 1065–1081, Feb. 2019.

[24] Z. Fang, Z. Wei, Z. Huang, and F. Liu, "Onboard energy storage system based on interleaved high-conversion-ratio quasi-resonant converter with small characteristic impedance," *IEEE Trans. Veh. Technol.*, vol. 70, no. 5, pp. 4238–4251, May 2021.

[25] R. Haneda and H. Akagi, "Design and performance of 850 V. 100 kW 16 kHz bidirectional isolated DC-DC converter using Sic-MOSFET/SBD H-bridge modules," *IEEE Trans. Power Electron.*, vol. 35, no. 10, pp. 10013–10025, Oct. 2020.

[26] G. B. Joung, C. T. Rim, and G. H. Cho, "Integral cycle mode control of series resonant converter," *IEEE Trans. Power Electron.*, vol. 4, no. 1, pp. 83–91, Jan. 1989.

[27] G. G. Oggier and M. Ordonez, "High-efficiency DAB converter using switching sequences and burst mode," *IEEE Trans. Power Electron.*, vol. 31, no. 3, pp. 2069–2082, Mar. 2016.

[28] H. Fujita and H. Akagi, "Control and performance of a pulse-density-modulated series-resonant inverter for corona discharge processes," *IEEE Trans. Ind. Appl.*, vol. 35, no. 3, pp. 621–627, May/Jun. 1999.

[29] H. Zeng, N. S. Geonzalez-Santini, Y. Yu, S. Yang, and F. Peng, "Harmonic burst control strategy for full-bridge series-resonant converter-based EV charging," *IEEE Trans. Power Electron.*, vol. 32, no. 5, pp. 4064–4073, May 2017.

[30] J. E. Huber, J. Minibock, and J. W. Kolar, "Generic derivation of dynamic model for half-cycle DCM series resonant converters," *IEEE Trans. Power Electron.*, vol. 33, no. 1, pp. 4–7, Jan. 2018.

[31] K. Venkatachalam, C. R. Sullivan, T. Abdallah, and H. Tacca, "Accurate prediction of ferrite core loss with nonsinusoidal waveforms using only Steinmetz parameters," in *Proc. 8th IEEE Workshop Comput. Power Electron.*, Mayaguez, Puerto Rico, 2002, pp. 1093–5142.

[32] Y. Zhang, D. Zhang, J. Li, and H. Zhu, "Bidirectional LCLL resonant converter with wide output voltage range," *IEEE Trans. Power Electron.*, vol. 35, no. 11, pp. 11813–11826, Apr. 2020.

[33] Y. Wang, B. Chen, Y. Hou, Z. Meng, and Y. Yang, "Analysis and design of a 1-MHz bidirectional multi-CLLC resonant DC–DC converter with GaN devices," *IEEE Trans. Ind. Electron.*, vol. 67, no. 2, pp. 1425–1434, Feb. 2020.

[34] J. Wu, P. Wen, X. Sun, and X. Yan, "Reactive power optimization control for bidirectional dual-tank resonant DC-DC converters for fuel cells systems," *IEEE Trans. Power Electron.*, vol. 35, no. 9, pp. 9202–9214, Sep. 2020.

Zhijian Fang (Member, IEEE) received the B.S. and Ph.D. degrees in electrical engineering and automation from the Huazhong University of Science and Technology, Wuhan, China, in 2010 and 2015, respectively.

From 2015 to 2018, he was a Postdoctoral Research Fellow with the School of Electrical Engineering, Wuhan University, Wuhan. From 2016 to 2017, he was a Postdoctoral Research Fellow with the Department of Electrical and Computer Engineering, Ryerson University, Toronto, ON, Canada. Since 2019, he has been a Professor with the School of Automatic, China University of Geosciences, Wuhan. His research interests include high performance dc/dc converter, battery charger, and renewable energy applications.

Hanlin Dong received the bachelor's degree in automation from South-Central Minzu University, Wuhan, China, in 2020. He is currently working toward the master's degree in control engineering with the China University of Geosciences, Wuhan.

His research focuses on integrated energy system optimization.

Haotian Sun received the bachelor's degree in automation from the Xinjiang Institute of Engineering, Ürümqi, China, in 2018. He is currently working toward the master's degree in control engineering with the China University of Geosciences, Wuhan, China.

He studies and works in the New Energy Laboratory. His research interests include computer vision and its applications in power systems.

Fei Xie received the bachelor's degree in automation in 2019 from the China University of Geosciences, Wuhan, China, where he is currently working toward the master's degree in control engineering.

His research focuses on power electronic converter and wireless power transmission.

Zhicong Huang (Member, IEEE) received the B.Eng. degree in electrical engineering and automation and the M.Eng. degree in mechanical and electronic engineering from the Huazhong University of Science and Technology, Wuhan, China, in 2010 and 2013, respectively, and the Ph.D. degree in power electronics from The Hong Kong Polytechnic University, Hong Kong, in 2018.

From 2019 to 2020, he was a Postdoctoral Fellow under the UM Macao Talent Program, with the State Key Laboratory of Analog and Mixed-Signal VLSI, University of Macau, Macao, China. He is currently an Associate Professor with the Shien-Ming Wu School of Intelligent Engineering, South China University of Technology, Guangzhou, China. His research interests include wireless power transfer, power electronics penetrated power system, electric vehicle, and intelligent engineering.

Dr. Huang was the recipient of the Outstanding Reviewer Award from IEEE TRANSACTIONS ON POWER ELECTRONICS in 2021.